DTU Library

The Melting Curve of Nickel Up to 100 GPa Explored by XAS

Boccato, Silvia; Torchio, Raffaella; Kantor, Innokenty; Morard, Guillaume; Anzellini, Simone; Giampaoli, Ruggero; Briggs, Richard; Smareglia, Alessandro; Irifune, Tetsuo; Pascarelli, Sakura

The Melting Curve of Nickel Up to 100 GPa Explored by XAS

Silvia Boccato[1] (ID)**, Raffaella Torchio[1], Innokenty Kantor[1,2], Guillaume Morard[3]** (ID)**, Simone Anzellini[4]** (ID)**, Ruggero Giampaoli[1,5]** (ID)**, Richard Briggs[1], Alessandro Smareglia[1,5], Tetsuo Irifune[6], and Sakura Pascarelli[1]**

[1] ESRF-European Synchrotron Radiation Facility, Grenoble, France, [2] Department of Physics, Technical University of Denmark, Kgs. Lyngby, Denmark, [3] Institut de Minéralogie, de Physique des Matériaux, et de Cosmochimie (IMPMC), Sorbonne Universités - UPMC, UMR CNRS 7590, Muséum National d'Histoire Naturelle, IRD UMR 206, F-75005, Paris, France, [4] Diamond Light Source Ltd, Didcot, UK, [5] Department of Physics, Politecnico di Milano, Milan, Italy, [6] Geodynamics Research Center, Ehime University, Matsuyama, Japan

Abstract Precise knowledge of the melting temperatures of iron, nickel, and their alloys at pressures of the deep Earth would allow us to better constrain the parameters used for the Earth's heat budget and dynamics. However, melting curves of transition metals at pressures approaching 100 GPa and above are still controversial. To address this issue, we report new data on the melting temperature of nickel in a laser-heated diamond anvil cell up to 100 GPa obtained by X-ray absorption spectroscopy (XAS), a technique rarely used at such conditions. We couple this for the first time to ex situ analysis of the sample, providing a further validation of the melting criterion adopted here. Finally, a Simon-Glatzel fit to the melting data obtained in this work, combined with those obtained in the most recent X-ray diffraction experiments, gives $T_M(K) = 1727 \times \left[\frac{P_M}{17 \pm 3} + 1 \right]^{\frac{1}{2.5 \pm 0.1}}$, defining the most up-to-date X-ray-determined melting curve for Ni. This result confirms that Ni could be ignored in the discussion on melting properties and thermal profile of the Earth's core, as it should affect the Fe melting point by only 10 – 20 K at 90 GPa.

1. Introduction

Planetary cores in the solar system are constituted of Fe alloyed with Ni and lighter elements, such as silicon, sulfur, carbon, oxygen, and hydrogen (Hirose et al., 2013; Poirier, 1994). The way these elements can affect the properties of pure Fe (phase diagram, elastic properties, etc.) has been intensively studied, with the aim to combine seismic behavior of the Earth's core and mineral physics data on iron alloys to constrain the Earth's core composition and properties. Among the different physical phenomena studied, melting is important because it can shed light on planetary core thermal profiles and therefore inner core crystallization and magnetic field generation.

Few papers deal with the effect of Ni on pure Fe compared to the literature available for the light elements. The Clapyeron slope and location of the fcc to hcp transition seems to be only slightly affected by Ni (Komabayashi et al., 2012; Kuwayama et al., 2008). Ni was found to stabilize the bcc structure under Earth's core conditions (Dubrovinsky et al., 2007), but this has been ruled out by more recent experiments (Tateno et al., 2012). On the contrary, the effect of nickel on iron elasticity (Sakai et al., 2014) as well as on magnetic properties (Hausoel et al., 2017) seems to be important under extreme pressure and high temperature.

Controversies were also raised concerning the melting temperatures of Fe and Ni. Whereas melting experiments performed on iron alloys have shown a clear agreement despite the experimental technique and melting criteria applied (Morard et al., 2014), a large disagreement persists between melting curves of pure end-members, obtained using different experimental techniques, making this a still debated field (Anzellini et al., 2013; Aquilanti et al., 2015; Lord, Wood, et al., 2014, and references within). In view of the complexity of these measurements at high pressures and temperatures, discrepancies on melting curves can arise from systematic errors in the evaluation of pressure and temperature, in interpretation of small changes of the data due to melting, pressure- and temperature-induced chemical reactions that modify the state of the sample, etc.

In this study we focus on the melting properties of Ni. Several criteria have been used previously to detect the melting curve of Ni in laser-heated diamond anvil cell (LH-DAC) experiments: the direct observation of movements on the sample surface, X-ray diffraction (XRD) measurements, and slope changes of the temperature

versus laser power relation. Energy dispersive X-ray absorption spectroscopy (ED-XAS) has recently been proposed to detect the melting of transition metals (Aquilanti et al., 2015; Boehler et al., 2009) in LH-DAC experiments. Applying this technique to pure Fe, these authors highlighted significant differences with XRD measurements (Anzellini et al., 2013). The present study applies ED-XAS to determine the melting curve of pure Ni and finds excellent agreement with the previously determined XRD melting curve of Ni (Lord, Wood, et al., 2014), in contradiction with the conclusions drawn from the previous study on pure Fe (Aquilanti et al., 2015). These results reinforce the conclusion of a high melting temperature for a Fe-Ni alloy under Earth's core conditions. Therefore, the effect of Ni on melting of pure Fe, with a potential amount of 5–10 wt % (McDonough, 2003), could be neglected under Earth's core conditions in the case of a Fe-Ni solid solution.

1.1. Review of Experimental Techniques for the Determination of the Nickel Melting Curve

Here we review the experimental methods that have been used in the literature to detect the melting of nickel under extreme conditions and compare them to theoretical studies.

In the method based on visual observation of melting, the sample surface is illuminated with an visible laser beam (typically 512.5 nm from an Argon laser). The surface roughness of the sample creates an interference pattern that is commonly referred to as laser speckle. Upon heating, rapid and continuous movement of the laser speckle is associated with movement of the sample surface due to a melting as the sample becomes molten (Boehler, 2000; Errandonea, 2013, Errandonea et al., 2001; Japel et al., 2005; Lazor et al., 1993).

With X-ray diffraction, XRD measurements are recorded continuously as the sample temperature is gradually increased, obtaining information about the solid structure up to the melting point. The melting of the sample is identified by the first appearance of liquid diffuse scattering (LDS) in the XRD pattern (Lord et al., 2014; Salamat et al., 2014).

Melting can also be detected by the observation of a plateau in the temperature versus laser power curve (Lord, Wood, et al., 2014). The significance of this plateau was originally proposed to be a consequence of the latent heat of melting. This hypothesis was recently discarded given that the small size of the sample would give a latent heat of melting too small compared with the heat provided by the lasers (Geballe and Jeanloz, 2012; Lord, Wann, et al., 2014). Several other explanations have been proposed and are discussed in detail in Geballe and Jeanloz (2012).

The existing experimental and theoretical melting curves for nickel are shown in Figure 1. Among the experimental studies (dashed lines + markers) a discrepancy is observed of ∼700 K at 70 GPa between the melting curves detected by visual observation of the speckle and the other two criteria (XRD and plateau). A similar discrepancy was already observed in other studies for different metals such as iron, lead, and tantalum (Anzellini et al., 2013; Dewaele et al., 2007, 2010), where the melting curves obtained using the visual observation are often more shallow than the ones measured with X-ray diffraction. The validity of the visual observation to determine melting has therefore been questioned, and in recent XRD studies the speckle motion was proposed to be a signature of fast recrystallization of the solid rather than melting (Anzellini et al., 2013; Lord, Wood, et al., 2014).

Theoretical calculations have been performed on nickel using molecular dynamics (MD) (Bhattacharya et al., 2011; Cao et al., 2015; Koči et al., 2006; Luo et al., 2010; Zhang et al., 2014) and density functional theory (DFT) (Pozzo & Alfé, 2013). A generally good agreement is found between the theory and the experimental curves detected by XRD and the temperature plateau method, where MD calculations using the embedded atom method (EAM), with Mendelev's potentials (Zhang et al., 2014) and first-principle calculations based on density functional theory (Pozzo & Alfé, 2013), are the ones showing the best agreement.

Energy dispersive X-ray absorption spectroscopy (ED-XAS) has recently been proposed as a complementary technique to XRD in detecting the melting of transition metals (Aquilanti et al., 2015; Boehler et al., 2009; Torchio et al., 2016) in LH-DAC experiment. Due to its short-range order sensitivity, the local structure of a solid (amorphous or crystalline) and of a liquid is measured with similar accuracy. In addition, XAS is element selective, and although first applications focused on the simpler single-component system (Fe, Ni etc.), it is ideally suited for future investigation of the local structure around specific elements in multicomponent melts. Element selectivity also makes XAS particularly sensitive to detect chemical reactions that may occur during the experiment.

In the case of iron, a large discrepancy was found between the melting curves measured by XRD and by ED-XAS (Anzellini et al., 2013; Aquilanti et al., 2015). Possible reasons for this discrepancy are systematic errors
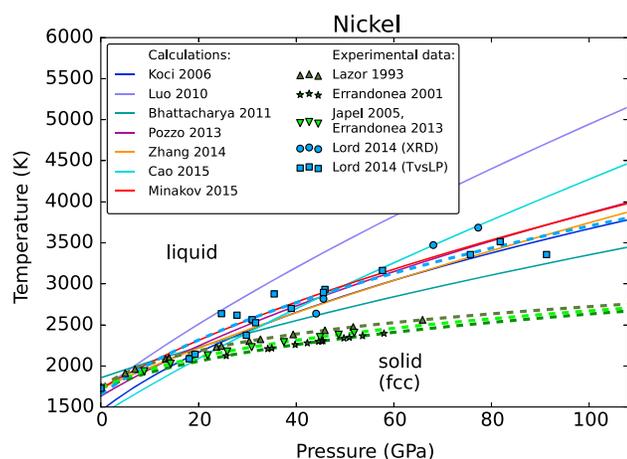
Figure 1. Nickel phase diagram. Comparison between experimental data (dashed lines + markers) measured with different techniques and from theoretical calculations (continuous lines). Experimental melting curves based on speckle melting criteria (Errandonea, 2013; Errandonea et al., 2001; Japel et al., 2005; Lazor et al., 1993) are at significantly lower temperatures than the XRD experimental curve of Lord, Wood, et al. (2014) — which is divided into melting points determined with XRD, blue circles, and with the temperature versus laser power plateau (TvsLP) points indicated with blue squares — and ab initio calculations (Bhattacharya et al., 2011; Cao et al., 2015; Koči et al., 2006; Luo et al., 2010; Pozzo & Alfé, 2013; Zhang et al., 2014).

in the temperature detection, sample modifications such as reactions, or misinterpretation of the solid-liquid transition signature. Systematic errors in the temperature measurement using refractive or reflective lenses, respectively used by Aquilanti et al. (2015) and Anzellini et al. (2013), have been recently investigated (Mezouar et al., 2017), pointing out that such a large discrepancy (900 K at 100 GPa) cannot be ascribed to the use of different optics. The effect of chemical reactions with the pressure medium and/or diamonds has been discussed for tantalum (Dewaele et al., 2010; Mezouar et al., 2017) and is still under investigation for the case of iron. Nickel is much less reactive than iron thus reducing the possible occurrence of chemical reactions (Lord, Wood, et al., 2014). The purpose of this study is to measure the Ni melting curve extending the knowledge of its phase diagram using XAS and to validate this method by ex situ post analysis of the laser-heated sample.

2. Methods

In this experiment, high pressure was generated using a membrane diamond anvil cell (DAC) with culet sizes ranging from a diameter of 150/300 μm (beveled diamonds) to 400 μm. Rhenium gaskets were preindented from an initial thickness of 200 μm down to 30–40 μm and laser drilled to create holes of the size of one third of the culet diameter. The sample, a 4 μm thick polycrystalline Ni foil 99.95% (Goodfellow), was loaded in the sample chamber together with a ruby chip and embedded between two KCl disks to be thermally insulated from the anvils. The KCl was previously dried in an oven at 120°C for at least 4 h, and the loading was performed in a glove bag fluxed with nitrogen in order to minimize the amount of water in the pressure transmitting medium (KCl). In fact it is known that water could trigger chemical reactions between the sample and the diamond anvils (Dewaele et al., 2010). Nanopolycrystalline diamonds were used in order to avoid the presence of Bragg peaks in the absorption spectrum (Ishimatsu et al., 2012).

During the experiment, two CW Nd:YAG fiber lasers (IPG photonics) with $\lambda = 1064$ nm, providing a maximum power of 120 W, were focused on both sides of the sample (Torchio et al., 2016). Temperature gradients, due to the Gaussian shape of the laser beams in the fundamental TEM$_{00}$ mode, were reduced by defocusing the beam. The resulting FWHM was 20 μm in diameter (vertically and horizontally), 2–3 times larger than the X-ray spot. X-ray absorption spectra at the Ni K-edge ($E_0 = 8333$ eV) were collected at the ED-XAS beamline ID24 at the ESRF (Pascarelli et al., 2016).

In the energy dispersive geometry at ID24, the X-ray beam is diffracted by an elliptically bent Si(111) crystal. Each X-ray energy has a different angle of diffraction, due to Bragg's law, and the geometry of the elliptically bent Si(111) crystal causes different positions of the crystal to diffract the different energies toward the sample, thereby focussing the beam horizontally Pascarelli et al. (2016). An additional silicon mirror is used to focus the beam vertically. The resulting beam size is ∼3×4 μm² (vertical x horizontal FWHM) in the 8310–8380 eV range, covering the region of Ni K-edge absorption spectrum which is sensitive to melting. The beam transmitted by the sample is recorded on a position sensitive detector, a FReLoN camera with an Hamamatsu chip (Kantor et al., 2014), where the position is correlated to the photon energy. Pixel to energy calibration is performed using a Ni standard reference. The whole XAS spectrum is thus obtained simultaneously allowing for fast collection of data. This is useful in laser heating experiments to reduce the sample exposure to the laser.
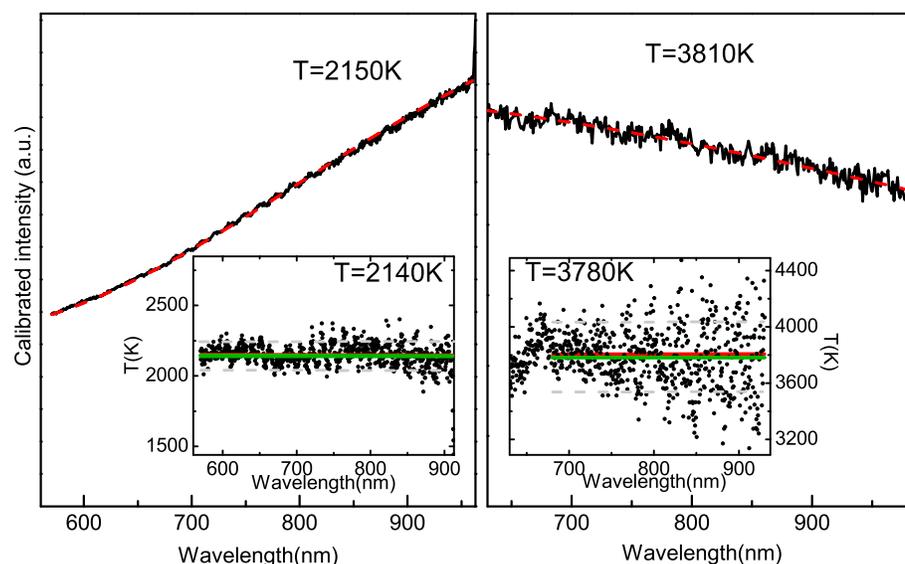
2.1. Temperature Determination

In these experiments, the temperature is determined using spectral-radiometry measurements. The thermal emission from the sample surface is collected through refractive optics and focused at the entrance of a Czerny-Turner type optical spectrometer with achromatic doublets embedded in a custom-built microscope and measured on a 1340 × 400 pixels Pixis 400B-EX back illuminated CCD camera (Torchio et al., 2016). The refractive microscopes have a numerical aperture of 0.2 that is reduced to 0.065 during temperature measurements by placing a pupil in front of the objective; this reduces the effect of chromatic aberrations. The optical path is calibrated using a temperature standard (tungsten lamp), after which the black body radiation

Figure 2. Example of Planck fit, in red, at 2150 K and 3810 K. In the inset the two color fits (Benedetti & Loubeyre, 2004) are shown with the mean temperature in green, in comparison with the result of the Planck fit in red. The gray dashed lines represent the variance of the distribution of temperatures around the mean value in the two-color plot.

of the hot spot is collected. Determination of the temperature, using spectroradiometry in the diamond anvil cell, can lead to large errors at very high temperatures. These errors are largely associated with not knowing the wavelength dependency of the emissivity; in the temperature fits we consider this to be constant. Furthermore, due to the Gaussian shape of the temperature profile of the heated spot, it is possible that during spectroradiometric measurements one could be probing different temperatures. In this study temperature errors are evaluated for each measurement by comparing the Planck's fit and the two-color fit, as described in Benedetti and Loubeyre (2004).

Temperatures are obtained as a result of Planck fits, adopting the gray body approximation, in a wavelength window ≥ 250 nm, where the two-color plot is almost flat, as shown in Figure 2. The temperature is then given by the average between the two sides of the heated sample, and its error is calculated as the standard deviation of the two-color fit. The difference in temperature between the two sides (50–100 K) is normally smaller than the standard deviation of the two-color fit (200–500 K); thus, it does not contribute to the error bar. As shown in Figure 2 the error bar becomes larger as the temperature increases.

2.2. Pressure Determination

The pressure is measured before and after heating by the ruby ($Cr:Al_2O_3$) fluorescence method, using the quasi-hydrostatic calibration of Mao (Mao et al., 1986). The thermal pressure correction is applied to the data exploiting the empirical relation $P_m = 0.03 \cdot P_{300}$ proposed by Lord, Wood, et al. (2014) for KCl, where P_m is the pressure at the melting temperature and P_{300} is the pressure measured on the ruby at room temperature after heating. If $T_0 = 300K$ and T_m is the melting temperature, the thermal pressure was evaluated as $P_{th} = \frac{0.03 \cdot P_{300}}{T_m - T_0}(T - T_0)$. The value of the pressure is then given by the sum of P_{th} and the pressure measured after heating. The main contribution to the error is given by the sample pressure variation that occurs during heating (of the order of 10%).

2.3. Measurement Strategy

When the required pressure is reached, the alignment of the spectral-radiometric optics and the X-rays is checked. This is crucial to ensure the collection of XAS and temperature data from the same spot on the sample. The alignment procedure is performed by optical visualization of the sample, the X-ray fluorescence of the KCl, and the pinhole situated at the entrance of the spectrometer. The image of the X-ray fluorescence is aligned on the pinhole (Mezouar et al., 2005), and this alignment is checked with X-rays using the gasket borders for knife-edge scans. Different regions of the sample are checked with the X-rays to find the best XAS signal. The lasers are then aligned on both sides of the chosen region and defocused in order to obtain a wide uniform hot spot around the selected spot.
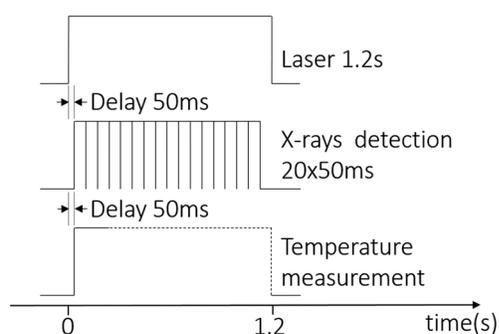
Figure 3. Synchronization scheme. The laser pulse lasts 1.2 s. During this time 10–20 spectra of 100–50 ms each are collected on the FReLoN X-ray camera starting with a delay of 50 ms after the onset of the laser pulse. The temperature is measured with an integration time that depends on the emitted intensity (it ranges from 1 s to 0.01 s).

Each heating run starts with a spectrum at room temperature and is followed by a sequence of alternating hot and quenched (to room temperature) spectra. The quenches allow tracking of possible changes in the sample due to chemical reactions or distortions of the sample. The laser power for each of the two lasers can be chosen independently as a fraction of the total laser power. The laser pulse, the XAS acquisition, and temperature measurement are synchronized by a trigger according to the scheme in Figure 3.

The acquisition time is chosen to optimize the signal to noise ratio for XAS measurements. Typically, an acceptable quality is obtained by averaging 10–20 acquisitions of 50–100 ms each. The laser pulse is therefore of the order of ~1 s, an interval sufficiently short to minimize chemical reactions. The temperature is measured independently from both sides of the cell, with an integration time varying according to the black body emission intensity: typically 1 s at 1500 K down to 0.01 s around 3000 K.

In order to prevent the probing of a region where the sample reacted or percolated through the pressure medium, the samples are heated at different positions after each heating ramp. An online analysis is carried out in order to track changes in the absorption spectrum of the hot sample; the laser power is then increased to reach the melting temperature. A delay of 50 ms between the laser onset and the XAS measurement is chosen to discard possible instabilities due to the sudden temperature variation.

3. Melt Criterion

In this study the onset of melting was determined in situ by observing the evolution of the X-ray absorption near edge structure (XANES) region of the collected spectra. An additional ex situ analysis was then performed using a focused ion beam (FIB) and a scanning electron microscope (SEM) on the recovered sample to confirm that melting had occured.

3.1. XAS

The XANES spectra were normalized setting to 0 the absorption just below the Ni K-edge, point E_b in Figure 4, and to 1 the absorption above the edge and immediately following the first two oscillations, point E_a in Figure 4. The following formula was used:

$$\mu_{\text{normalized}}(E) = \frac{\mu_{\text{raw}}(E) - \mu(E_b)}{\mu(E_a)}.$$

In the absorption spectra the transition from a solid to a liquid phase is identified by a clear change in the XANES region: the disappearing of the edge shoulder and the flattening of the first two bumps, as shown in Figure 4a. This change can also be detected in the derivative of the XANES, as shown in Figure 4a (top). Such changes in the XANES have already been used in the literature to detect the melting of Fe under pressure (Aquilanti et al., 2015), which is, like Ni, a transition metal with unfilled 3d bands. First theoretical validations of the above mentioned melting criterion were proposed for iron under extreme conditions (Harmand et al., 2015; Mazevet et al., 2014; Raji & Scandolo, 2014; Raji et al., 2013), where the disappearance of the shoulder in the XANES was shown to be due to the solid-liquid transition. The discontinuity observed in the absorption spectrum upon melting can be used to follow the phase transition as a function of temperature. This is the basis of the "single energy X-ray absorption temperature scan" method (T-scan method), used to investigate melting of Cu and Ni at ambient pressure (Di Cicco & Trapananti, 2007; Cicco et al., 2014). This method was validated for Ni at ambient pressure by collecting XRD patterns before and after melting showing total loss of long range order (Cicco et al., 2014).

An example of this method, applied to the data in this work, is represented in Figure 4b, where the variation of the absorption coefficient at point B ($E = 8338$ eV) is represented as a function of temperature. The sudden jump of the trend as a function of temperature represents the transition to the liquid phase. However, in some cases, probably due to thermal gradients, the melting signature appears gradually due to a solid/liquid coexistence in the sample. The T-scan method is very accurate if the XAS spectra are not deformed with temperature, but at the extreme pressures and temperatures used in this work, this is not always achieved and having the possibility to record the full energy range of the XAS spectrum is an asset in these difficult situations.
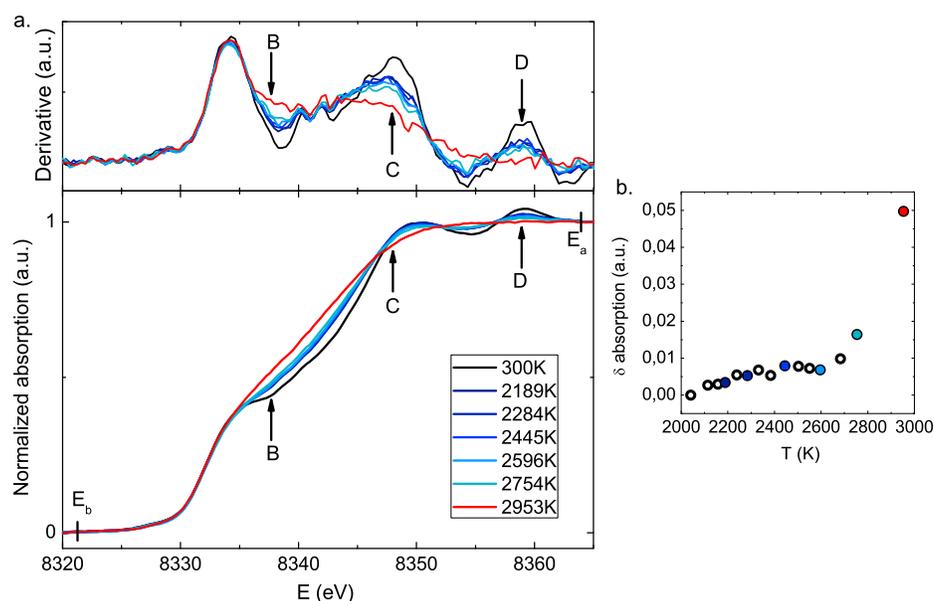
Figure 4. X-ray absorption spectroscopy melting criterion shown for nickel at 30 GPa. (a, bottom) The points E_b and E_a indicate where the normalization has been performed. The absorption at point E_b, below the edge, is set at 0, while the absorption at point E_a, above the edge, is set at 1. The melting criterion consists in the disappearance of the shoulder at point B and the flattening of the two oscillations at points C and D. This is also visible in (a, top) the derivative. The flattening of the derivative at points B, C, and D is a signature of melting. (b) The variation of the absorption as a function of temperature at point B ($E = 8338$ eV) is shown as a function of temperature with empty circles. The filled circles represent the spectra that are plotted in Figure 4a with the same color. A discontinuity appears in correspondence of the melting.

The changes in the edge region are due to the coexistence of a large number of different local atomic configurations forming in the liquid phase, also responsible for a broadening of the electronic bands around the Fermi energy (Mazevet et al., 2014). A deeper investigation on the physical phenomena that give rise to the XANES modification is currently ongoing and will be published elsewhere.

This melting criterion was applied in all the heating runs, and the temperature of the first spectrum showing these changes was considered as the melting temperature T_M. Most of the time, even if the laser power was increased slowly, the observed transition between solid and liquid was sharp and detection of melting is obvious.

3.2. Validation With FIB and SEM

In order to provide a further validation to the criterion for the case of Ni under extreme conditions of pressure and temperature, some of the samples were recovered after the experiment, and cross sections of the laser-heated hot spots were prepared by focused ion beam (FIB) milling. The exposed cross section has been imaged using the combined scanning electron microscope (SEM) (Zeiss Neon40ESB). The variation of shape is due to surface tension, which distinguishes the behavior of liquid from solid matter. This method has already been used to confirm the melting of tantalum and iron alloys (Karandikar & Boehler, 2016; Morard et al., 2017), where the shape and texture of the exposed spot reveal if the sample was molten or not. The shape of the cross section of a solid or liquid heated spot are indeed noticeably different (Figure 5a). Performing the cut at different depths gives an idea of the three-dimensional sample shape through the heated spot.

In the case of the solid, the borders of the sample foil remain the same as the unheated sample. The section of a liquid shows a significant unevenness with, very often, a nonuniform thickness. In Figure 5a the X-ray spot size is indicated in comparison with the laser spot size. The shape of the cut sample shows the size of the whole laser-heated area and can thus be used to infer the size of the laser. This represents approximately 3 times the X-ray beam size, minimizing temperature gradients in the measured X-ray spot area.

In both cases the section of the heated spot is surrounded by droplets of diffused nickel (see Figure 5b). The nature of these diffused droplets has been verified with energy dispersive spectrometry (EDS) analysis. The presence of these droplets helps in recognizing the heated spot even when the sample was a hot solid.
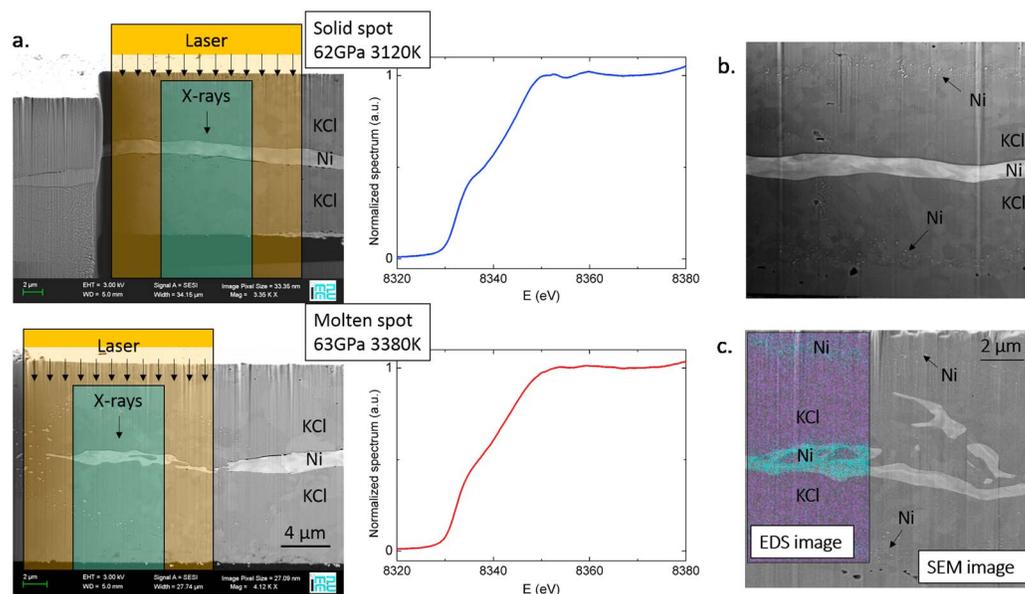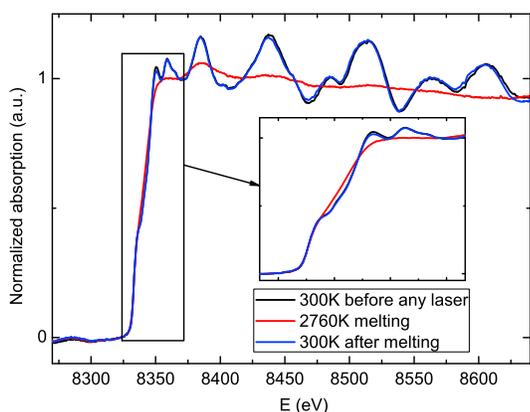
Figure 5. FIB and SEM melting criterion. (a, top left) In the first image the borders of the sample foil are intact, corresponding to heating temperature below the melting. (a, bottom left) A liquid with its characteristic irregular shape is shown. (a, right column) The corresponding XAS spectra for both images. (c) A SEM and an EDS image are superimposed to show the composition of the cut. Some nickel diffused from the sample by Soret effect (Sinmyo & Hirose, 2010) into the KCl both for (b) the solid and (c) the liquid heated spot.

Solid migration is due to the Soret effect (Sinmyo & Hirose, 2010). For the seven samples postanalyzed with this method, the observed features confirmed the corresponding XAS interpretations. In some cases the shape of the sample was only slightly deformed with respect to the solid, corresponding to a solid-liquid mix.

4. Results and Discussion
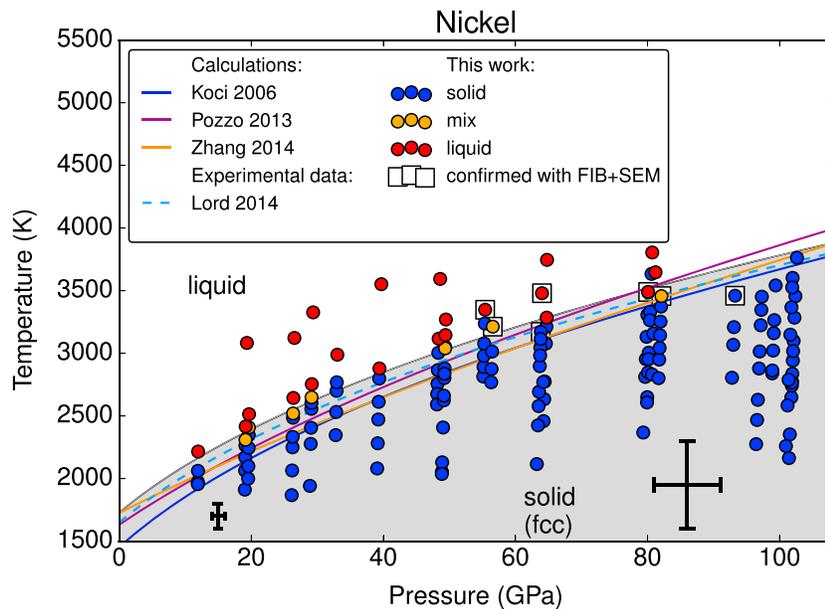
4.1. Melting Curve of Pure Nickel

The points of the pressure-temperature phase diagram probed in this study are illustrated in Figure 7. The criterion adopted to validate a melting cycle by XAS is that the near-edge spectrum of the sample before and after melting are exactly the same, showing that no chemical reaction or sample modification occurred during heating cycles. An example is plotted in Figure 6, where a XAS spectrum is shown before heating (black curve), during melting (red curve), and after melting (blue curve).

The temperatures for the solid/mix/melt at different pressures are indicated by blue/orange/red symbols in Figure 7. The white square symbols correspond to the P, T conditions for which the state of the sample was confirmed by means of the FIB + SEM method. This study is compared with previous experiments and calculations found in the literature. Within experimental error our data are in good agreement with the experimental data recently measured with XRD (Lord, Wood, et al., 2014) where in each heating run the sample was heated continuously for 5–15 min at increasing temperature. There is a very good agreement also with some of the theoretical works such as molecular dynamics simulations using the embedded atom method with Mendelev's potential (Zhang et al., 2014), first-principle calculations based on density functional theory (Pozzo & Alfé, 2013) and nonequilibrium molecular dynamics simulations to study shock-induced melting in nickel (Koči et al., 2006). A fit of the data to a Simon-Glatzel equation (Simon & Glatzel, 1929) gives

Figure 6. XAS spectra at 27 GPa before heating (black curve), during melting (red curve), and after the melting (blue curve). In the inset is shown a zoom of the XANES.

$$T_M(K) = 1728 \times \left[\frac{P_M}{15 \pm 3} + 1 \right]^{\frac{1}{2.60 \pm 0.02}}.$$

Figure 7. Nickel phase diagram measured by means of absorption spectroscopy. Blue, orange, and red symbols represent *P, T* conditions of solid, mixed, and liquid phases, respectively (the black cross with end bars corresponds to the error bars for the melting data). The white squares are the *P, T* conditions for which the state of the sample was confirmed by FIB+SEM post analysis. The curve dividing the gray and the white regions is the Simon-Glatzel fit of the data. Only experimental and theoretical works in agreement with our data set are presented (Koči et al., 2006; Lord et al., 2014; Pozzo & Alfé, 2013; Zhang et al., 2014).

The good agreement between the melting determined by XRD (Lord, Wood, et al., 2014) and this work shows that for nickel neither the heating method (continuous laser ramp or several short laser exposures), the optics used for the temperature measurement (reflective or refractive), nor the X-ray technique employed (XRD or XAS) introduce a technical bias in the determination of the melting temperature. With these techniques two different facets of the same process are measured: XRD detects melting through the loss of long-range order; with XAS melting is detected through the appearance of different local configurations. The only difference found between the results obtained using the two techniques, though, is that in XAS there is no signature of any fast recrystallization preceding the melting (as in Anzellini et al., 2013). This finding sheds light on the important discrepancy (800–1000 K) found for the iron case in similar experiments: XRD in continuous heating, where the temperature was measured using reflective optics (Anzellini et al., 2013), and XAS in pulsed heating, where the *T* was measured using refractive optics (Aquilanti et al., 2015). Therefore, the origin of this disagreement has to be found in other experimental aspects. Our melting measurements are in very good agreement over the entire pressure range between XRD and XAS measurements, confirming the complementarity between the two melting detection methods.

As a result, we merge the results obtained in this work with those measured in the paper by Lord, Wood, et al. (2014). The Simon-Glatzel fit of the merged data gives

$$T_M(K) = 1,727 \times \left[\frac{P_M}{17 \pm 3} + 1 \right]^{\frac{1}{2.5 \pm 0.1}},$$

thus providing the most up-to-date X-ray-determined melting curve for Ni.

4.2. Implications for the Fe-Ni Solid Solution

We now compare our experimentally determined melting curve of Ni to that of pure Fe. At 90 GPa, melting of pure Fe is expected to be at 3440 K Anzellini et al. (2013). The present data set gives us a melting temperature of 3650 K at 90 GPa for pure Ni. Assuming a linear relation between the two end-members, as supported by the existence of solid solution in the Fe-Ni binary system Kuwayama et al. (2008), we obtain an increase of 2 K/wt % Ni of the melting temperature of pure Fe; therefore, the effect of Ni may be to increase the melting temperature of the Earth's core of ~10–20 K (Ni content ~5–10 wt %). This is 1 order of magnitude lower than the effect of light element such as S, C, or O Morard et al. (2017) at 90 GPa and in the opposite direction.

Above 90 GPa, Fe adopts the hcp structure, whereas Ni remains in the fcc structure. The two phases (hcp + fcc) have the same packing factor, and therefore this change in structure is not expected to change significantly our findings. We can therefore conclude that the effect of Ni could be significantly smaller than that of light elements in the discussion of temperature and melting relations in the Earth's core.

As an outlook for future work, now that XAS has been established as a valuable means to investigate the P and T phase diagrams of pure Fe and Ni, its element selectivity could be exploited to explore the Fe-Ni alloy phase diagram at the two edges, to provide insight into the electronic and local structure, complementary to XRD. Recent ab initio DFT calculations on Fe-Ni alloys at conditions representative of the Earth's inner core (Côté et al., 2012) predict phase stability boundaries which call for experimental evidence.

5. Conclusions

In this study the melting curve of nickel up to 100 GPa has been measured by ED-XAS in LH-DAC. The adopted melting criterion was the observation of changes in the XANES region of the spectra, namely, the disappearance of the shoulder and the flattening of the first two oscillations. This criterion has been applied and validated for nickel with an ex situ post analysis, which consisted of cutting the quenched sample with FIB and looking at the shape of the heated spots with SEM. An interesting outlook for the future could be the design of a laser heating system allowing the detection of combined XAS and XRD.

This melting curve is in good agreement with a large number of calculations, namely, the ones involving DFT and MD with EAM, and with the most recent diffraction measurements. These results illustrate that determination of melting at high pressure does not depend on the X-ray technique used (XRD and XAS) nor on the optics employed for the temperature determination (reflective or refractive), as already shown in Lord, Wood, et al. (2014).

Linear interpolation in the Fe-Ni solid solution gives an increase of 10–20 K for Fe melting temperature due to the addition of Ni in the Earth's core, 1 order of magnitude lower than the effect of light elements (Morard et al., 2017) and in the opposite direction. Nickel could then be neglected during discussion of temperature profile and melting relations under Earth's core conditions.

References

Anzellini, S., Dewaele, A., Mezouar, M., Loubeyre, P., & Morard, G. (2013). Melting of iron at Earth's inner core boundary based on fast X-ray diffraction. *Science*, *340*(6131), 464–6.

Aquilanti, G., Trapananti, A., Karandikar, A., Kantor, I., Marini, C., Mathon, O., … Boehler, R. (2015). Melting of iron determined by X-ray absorption spectroscopy to 100 GPa. *Proceedings of the National Academy of Sciences*, *112*(39), 12,042–12,045.

Benedetti, L., & Loubeyre, P. (2004). Temperature gradients, wavelength-dependent emissivity, and accuracy of high and very-high temperatures measured in the laser-heated diamond cell. *High Pressure Research*, *24*(4), 423–445.

Bhattacharya, C., Srivastava, M. K., & Menon, S. V. G. (2011). Melting curves of fcc-metals by cell-theory. *Physica B: Physics of Condensed Matter*, *406*(21), 4035–4040.

Boehler, R. (2000). High-pressure experiments and the phase diagram of lower mantle and core materials. *Reviews of Geophysics*, *38*(1998), 221–245. https://doi.org/10.1029/1998RG000053

Boehler, R., Musshoff, H. G., Ditz, R., Aquilanti, G., Trapananti, A., Boehler, R., … System, I. I. L.-H. (2009). Portable laser-heating stand for synchrotron applications. *Review of Scientific Instruments*, *80*, 045103.

Cao, Q.-L., Wang, P.-P., Huang, D.-H., Yang, J.-S., Wan, M.-J., & Wang, F.-H. (2015). Properties of liquid nickel along melting lines under high pressure. *Chinese Physics Letters*, *32*(8), 086201.

Cicco, A. D., Iesari, F., De Panfilis, S., Celino, M., Giusepponi, S., & Filipponi, A. (2014). Local fivefold symmetry in liquid and undercooled Ni probed by X-ray absorption spectroscopy and computer simulations. *Physical Review B - Condensed Matter and Materials Physics*, *89*, 060102.

Côté, A. S., Vocadlo, L., & Brodholt, J. P. (2012). Ab initio simulations of iron nickel alloys at Earth's core conditions. *Earth and Planetary Science Letters*, *345–348*, 126–130.

Dewaele, A., Mezouar, M., Guignot, N., & Loubeyre, P. (2007). Melting of lead under high pressure studied using second-scale time-resolved X-ray diffraction. *Physical Review B - Condensed Matter and Materials Physics*, *76*(14), 1–5. https://doi.org/10.1103/PhysRevB.76.144106

Dewaele, A., Mezouar, M., Guignot, N., & Loubeyre, P. (2010). High melting points of tantalum in a laser-heated diamond anvil cell. *Physical Review Letters*, *104*(25), 29–31.

Di Cicco, A., & Trapananti, A. (2007). Study of local icosahedral ordering in liquid and undercooled liquid copper. *Journal of Non-Crystalline Solids*, *353*(32–40), 3671–3678.

Dubrovinsky, L. S., Dubrovinskaia, N. A., Narygina, O., Kantor, I., Kuznetsov, A. Y., Prakapenka, V. B., … Abrikosov, I. A. (2007). Body-centered cubic iron-nickel alloy in Earth's core. *Science*, *316*, 1880–1884.

Errandonea, D. (2013). High-pressure melting curves of the transition metals Cu, Ni, Pd, and Pt. *Physical Review B - Condensed Matter and Materials Physics*, *87*(5), 1–5. https://doi.org/10.1103/PhysRevB.87.054108

Errandonea, D., Schwager, B., Ditz, R., Gessmann, C., Boehler, R., & Ross, M. (2001). Systematics of transition-metal melting. *Physical Review B - Condensed Matter and Materials Physics*, *63*(13), 132104.

Geballe, Z. M., & Jeanloz, R. (2012). Origin of temperature plateaus in laser-heated diamond anvil cell experiments. *Journal of Applied Physics*, *111*(12), 123518.

Harmand, M., Ravasio, A., Mazevet, S., Bouchet, J., Denoeud, A., Dorchies, F., … Benuzzi-Mounaix, A. (2015). X-ray absorption spectroscopy of iron at multimegabar pressures in laser shock experiments. *Physical Review B - Condensed Matter and Materials Physics*, *92*(024108), 1–7.

Hausoel, A., Karolak, M., Sasioglu, E., Lichtenstein, A., Held, K., Katanin, A., … Sangiovanni, G. (2017). Local magnetic moments in iron and nickel at ambient and Earth's core conditions. *Nature communications*, *8*(16062), 1–9. https://doi.org/10.1038/ncomms16062

Hirose, K., Labrosse, S., & Hernlund, J. (2013). Composition and state of the core. *Annual Review of Earth and Planetary Sciences*, *41*(1), 657–691. https://doi.org/10.1146/annurev-earth-050212-124007

Ishimatsu, N., Matsumoto, K., Maruyama, H., Kawamura, N., Mizumaki, M., Sumiya, H., & Irifune, T. (2012). Glitch-free X-ray absorption spectrum under high pressure obtained using nano-polycrystalline diamond anvils. *Journal of Synchrotron Radiation*, *19*(5), 768–772.

Japel, S., Schwager, B., Boehler, R., & Ross, M. (2005). Melting of copper and nickel at high pressure: The role of d electrons. *Physical Review Letters*, *95*(16), 1–4.

Kantor, I., Labiche, J.-C., Collet, E., Siron, L., Thevenin, J.-J., Ponchut, C., … Pascarelli, S. (2014). A new detector for sub-millisecond EXAFS spectroscopy at the European Synchrotron Radiation Facility. *Journal of Synchrotron Radiation*, *21*(6), 1240–1246.

Karandikar, A., & Boehler, R. (2016). Flash melting of tantalum in a diamond cell to 85 GPa. *Physical Review B*, *93*(054107), 1–6.

Koči, L., Bringa, E. M., Ivanov, D. S., Hawreliak, J., McNaney, J., Higginbotham, A., … Ahuja, R. (2006). Simulation of shock-induced melting of Ni using molecular dynamics coupled to a two-temperature model. *Physical Review B - Condensed Matter and Materials Physics*, *74*(1), 2–5. https://doi.org/10.1103/PhysRevB.74.012101

Komabayashi, T., Hirose, K., & Ohishi, Y. (2012). In situ X-ray diffraction measurements of the fcc hcp phase transition boundary of an Fe Ni alloy in an internally heated diamond anvil cell. *Physics and Chemistry of Minerals*, *39*, 329–338. https://doi.org/10.1007/s00269-012-0490-3

Kuwayama, Y., Hirose, K., Sata, N., & Ohishi, Y. (2008). Phase relations of iron and iron-nickel alloys up to 300 GPa: Implications for composition and structure of the Earth's inner core. *Earth and Planetary Science Letters*, *273*(3–4), 379–385. https://doi.org/10.1016/j.epsl.2008.07.001

Lazor, P., Shen, G., & Saxena, S. K. (1993). Laser-heated diamond anvil cell experiments at high pressure: Melting curve of nickel up to 700 kbar. *Physics and Chemistry of Minerals*, *20*(2), 86–90.

Lord, O., Wood, I., Dobson, D., Vocadlo, L., Wang, W., Thomson, A., … Walter, M. (2014). The melting curve of Ni to 1 Mbar. *Earth and Planetary Science Letters*, *408*, 226–236.

Lord, O. T., Wann, E. T. H., Hunt, S. A., Walker, A. M., Santangeli, J., Walter, M. J., … Mezouar, M. (2014). The NiSi melting curve to 70 GPa. *Physics of the Earth and Planetary Interiors*, *233*, 13–23. https://doi.org/10.1016/j.pepi.2014.05.005

Luo, F., Chen, X. R., Cai, L. C., & Ji, G. F. (2010). Solid-liquid interfacial energy and melting properties of nickel under pressure from molecular dynamics. *Journal of Chemical and Engineering Data*, *55*(11), 5149–5155.

Mao, H. K., Xu, J., & Bell, P. M. (1986). Calibration of the ruby pressure gauge to 800 kbar under quasi-hydrostatic conditions. *Journal of Geophysical Research*, *91*(B5), 4673–4676.

Mazevet, S., Recoules, V., Bouchet, J., Guyot, F., Harmand, M., Ravasio, A., & Benuzzi-Mounaix, A. (2014). Ab initio calculation of X-ray absorption of iron up to 3 Mbar and 8000 K. *Physical Review B - Condensed Matter and Materials Physics*, *89*(10), 1–5.

McDonough, W. F. (2003). Compositional model for the Earth's core, *Treatise on Geochemistry* (Vol. 2, pp. 547–568). Amsterdam: Elsevier.

Mezouar, M., Crichton, W. A., Bauchau, S., Thurel, F., Witsch, H., Torrecillas, F., … Borel, C. (2005). Development of a new state-of-the-art beamline optimized for monochromatic single-crystal and powder X-ray diffraction under extreme conditions at the ESRF. *Journal of Synchrotron Radiation*, *12*(5), 659–664.

Mezouar, M., Giampaoli, R., Garbarino, G., Kantor, I., Dewaele, A., Weck, G., … Bauchau, S. (2017). Methodology for in situ synchrotron X-ray studies in the laser-heated diamond anvil cell. *High Pressure Research*, *37*, 170–180.

Morard, G., Andrault, D., Antonangeli, D., & Bouchet, J. (2014). Properties of iron alloys under the Earth's core conditions. *Comptes Rendus Geoscience*, *346*(5–6), 130–139.

Morard, G., Andrault, D., Antonangeli, D., Nakajima, Y., Auzende, A., Boulard, E., … Mezouar, M. (2017). Fe-FeO and Fe-Fe3C melting relations at Earth's core mantle boundary conditions: Implications for a volatile-rich or oxygen-rich core. *Earth and Planetary Science Letters*, *473*, 94–103.

Pascarelli, S., Mathon, O., Mairs, T., Kantor, I., Agostini, G., Strohm, C., … Dominguez, M. C. (2016). The Time-resolved and Extreme-conditions XAS (TEXAS) facility at the European Synchrotron Radiation Facility: The energy-dispersive X-ray absorption spectroscopy beamline ID24. *Journal of Synchrotron Radiation*, *23*(1), 353–368.

Poirier, J.-P. (1994). Light elements in the Earth's outer core: A critical review. *Physics of the Earth and Planetary Interiors*, *85*(94), 319–337.

Pozzo, M., & Alfé, D. (2013). Melting curve of face-centered-cubic nickel from first-principles calculations. *Physical Review B - Condensed Matter and Materials Physics*, *88*, 024111. https://doi.org/10.1103/PhysRevB.88.024111

Raji, A., & Scandolo, S. (2014). Theoretical X-ray absorption near-edge structure signatures of solid and liquid phases of iron at extreme conditions. *High Pressure Research*, *34*(2), 250–258.

Raji, A. T., Scandolo, S., Härting, M., & Britton, D. T. (2013). Probing the structure of iron at extreme conditions by X-ray absorption near-edge structure calculations. *High Pressure Research*, *33*(1), 119–123.

Sakai, T., Takahashi, S., Nishitani, N., Mashino, I., Ohtani, E., & Hirao, N. (2014). Equation of state of pure iron and Fe0.9Ni0.1 alloy up to 3 Mbar. *Physics of the Earth and Planetary Interiors*, *228*, 114–126. https://doi.org/10.1016/j.pepi.2013.12.010

Salamat, A., Fischer, R. A., Briggs, R., McMahon, M. I., & Petitgirard, S. (2014). In situ synchrotron X-ray diffraction in the laser-heated diamond anvil cell: Melting phenomena and synthesis of new materials. *Coordination Chemistry Reviews*, *277*, 15–30.

Simon, F., & Glatzel, G. (1929). Bemerkungen zur Schmelzdruckkurve. *Zeitschrift für Anorganische und Allgemeine Chemie*, *178*, 309–316.

Sinmyo, R., & Hirose, K. (2010). The Soret diffusion in laser-heated diamond-anvil cell. *Physics of the Earth and Planetary Interiors*, *180*(3–4), 172–178.

Tateno, S., Hirose, K., Komabayashi, T., Ozawa, H., & Ohishi, Y. (2012). The structure of Fe-Ni alloy in Earth's inner core. *Geophysical Research Letters*, *39*, L12305. https://doi.org/10.1029/2012GL052103

Torchio, R., Boccato, S., Cerantola, V., Morard, G., Irifune, T., & Kantor, I. (2016). Probing the local, electronic and magnetic structure of matter under extreme conditions of temperature and pressure. *High Pressure Research*, *36*(3), 293–302.

Zhang, W.-j., Liu, Z.-l., & Peng, Y.-f. (2014). Molecular dynamics simulations of the melting curves and nucleation of nickel under pressure. *Physica B - Physics of Condensed Matter*, *449*, 144–149.